ResearchGate

See discussions, stats, and author profiles for this publication at: https://www.researchgate.net/publication/335238927

Interactive promotion of supercapacitance of rare earth/CoO3-based spray pyrolytic perovskite microspheres hosting the hydrothermal ruthenium oxide

Article *in* Electrochimica Acta · August 2019

DOI: 10.1016/j.electacta.2019.134721

CITATIONS
3

READS
37

7 authors, including:

Sanja Erakovic
Institute for Chemistry, Technology and Metallurgy, University of Belgrade
25 PUBLICATIONS **732** CITATIONS
SEE PROFILE

Miroslav M. Pavlovic
University of Belgrade
41 PUBLICATIONS **150** CITATIONS
SEE PROFILE

Srećko Stopić
RWTH Aachen University
197 PUBLICATIONS **1,529** CITATIONS
SEE PROFILE

Jasmina Stevanović
Institute of Chemistry, Technology and Metallurgy, University of Belgrade
168 PUBLICATIONS **1,385** CITATIONS
SEE PROFILE

Some of the authors of this publication are also working on these related projects:

Electronic Scrap Recycling View project

Circular economy (recycling processes) for batteries View project

All content following this page was uploaded by Miroslav M. Pavlovic on 01 September 2019.

The user has requested enhancement of the downloaded file.

Electrochimica Acta 321 (2019) 134721

Contents lists available at ScienceDirect

Electrochimica Acta

journal homepage: www.elsevier.com/locate/electacta

Interactive promotion of supercapacitance of rare earth/CoO_3-based spray pyrolytic perovskite microspheres hosting the hydrothermal ruthenium oxide

Sanja Eraković [a], Miroslav M. Pavlović [a, *], Srećko Stopić [b], Jasmina Stevanović [a, c], Miodrag Mitrić [d], Bernd Friedrich [b], Vladimir Panić [a, c, e, **]

[a] Institute of Chemistry, Technology and Metallurgy, Department of Electrochemistry, University of Belgrade, Njegoševa 12, Belgrade, Serbia
[b] Process Metallurgy and Metal Recycling, RWTH Aachen University, Intzestraße 3, Aachen, Germany
[c] Centre of Excellence in Environmental Chemistry and Engineering - ICTM, University of Belgrade, Njegoševa 12, Belgrade, Serbia
[d] Vinča Institute of Nuclear Sciences, University of Belgrade, 12-14 Mike Petrovića Street, Belgrade, Serbia
[e] State University of Novi Pazar, Department of Chemical-Technological Sciences, Novi Pazar, Serbia

ARTICLE INFO

Article history:
Received 22 April 2019
Received in revised form
23 July 2019
Accepted 17 August 2019
Available online 19 August 2019

Keywords:
Capacitor electrodes
Oxide composites
Rare earths
Electrocatalytic interactivity
Supercapacitive material

ABSTRACT

Considerable promotion of RuO_2 hosted by perovskite-like structure of rare earth—CoO_3 composite and *vice versa* supercapacitive performances is reported. Spherical, sub-μm-sized, regular spheres of $La_{0.6}Sr_{0.4}CoO_3$ (LSCO), were synthesized by ultrasonic spray pyrolysis. The sphere surface was subsequently hydrothermally doped by RuO_2. LSCO and LSCO/RuO_2 composites were investigated for their supercapacitive performances in alkaline solution. Microstructure and surface morphology were studied by SEM and XRD. It was found that amorphous Ru species decorate LSCO surface, and possibly incorporate partially into B-site of the LSCO lattice. Electrochemical characterization by cyclic voltammetry (CV), galvanostatic charge-discharge (G-C/DC) and electrochemical impedance spectroscopy (EIS) clearly revealed that capacitive performances of LSCO are considerably improved by addition of 20 mass. % of RuO_2. The registered capacitance for LSCO/RuO_2 reaches the values of pure RuO_2, which reveals the promoting influence of LSCO on RuO_2 pseudocapacitance. The EIS analysis showed that RuO_2 catalyzes the redox transition of Co species, with simultaneous proportional increase in pseudocapacitive RuO_2 abilities while being hosted by LSCO. This intrinsic interactive promotion introduces LSCO/RuO_2 composite as unique supercapacitive material. G-C/DC curves showed that LSCO/RuO_2 is of modest cyclability with respect to pure LSCO and RuO_2, although the capacitance losses with cycling are acceptably low.
© 2019 Elsevier Ltd. All rights reserved.

1. Introduction

In recent years, huge research efforts in investigation of novel materials used in electrochemistry-based energy storage processes are triggered [1]. Supercapacitors, as a bridge between batteries and traditional capacitors, have attracted significant attention as new promising energy storage devices [1–3]. Supercapacitor delivers high power densities (about 1–100 kW kg^{-1}) for a given energy density (of a device being classified as capabattery) and long cyclability (10^5~10^6 cycles) while charges/discharges in high rates with respect to batteries [1,2,4,5].

Transition metal oxides (TMOs) are considered as an ideal electrode materials for electrochemical redox transitions-based pseudocapacitors (EPCs), because they can provide a variety of oxidation states for rather fast and efficient redox transitions [6]. Among the electroactive materials used for EPCs, hydrous RuO_2 was identified as an excellent candidate because of its high theoretical specific capacitance (1358 Fg^{-1}), electrical conductivity (300 Scm^{-1}) and high electrochemical stability [1,7,8]. However, the commercial application of RuO_2 is questionable due to its high cost, low porosity, and toxicity associated with Ru [6,7]. Numerous new materials have been widely designed and prepared to overcome this issue [9–13]. One possible way to reduce costs is the partial substitution of Ru species in a different types of oxide structures [7].

* Corresponding author. Department of Electrochemistry, Institute of Chemistry, Technology and Metallurgy University of Belgrade, Serbia.
** Corresponding author. Institute of Chemistry, Technology and Metallurgy, Department of Electrochemistry, University of Belgrade, Njegoševa 12, Belgrade, Serbia.
E-mail address: mpavlovic@tmf.bg.ac.rs (M.M. Pavlović).

https://doi.org/10.1016/j.electacta.2019.134721
0013-4686/© 2019 Elsevier Ltd. All rights reserved.

Rare earth ruthenates with perovskite structure of the general formula ABO_3 (where A-lanthanide, B-transition metal) containing ruthenium in the B-site position have been shown to exhibit pseudocapacitance behavior [7,14]. Furthermore, some perovskite materials based on cobalt oxide are considered to be valuable with regard to energy device applications due to their mixed proton/electron conductivity [15]. Perovskites containing Ru on the B position have been shown to exhibit pseudocapacitive behavior and metallic conductivity [7,16]. These mixed conductors are synthesized in various material combinations [14,17,18], including strontium-doped lanthanum cobaltites ($La_{1-x}Sr_xCoO_{3-\delta}$, LSCO) [15], which are one of the most promising perovskite compounds (containing La and Sr cations on A-sites with Co cations on B-sites) due high electrochemical stability and fast charge/discharge rates [15].

$La_{1-x}Sr_xCoO_{3-\delta}$ films can be prepared by different techniques, like sol-gel method, spin coating, dipping-pyrolysis, vapor deposition, *etc*. Spray pyrolysis was found to be of several advantages: low cost, flexibility, convenience for large deposition area and capability for preparing nanostructured thin films [17–19]. There are literature reports about promising synthesis of perovskite materials by ultrasonic spray pyrolysis (USP). Perovskite material is known for being able to improve the performance of solid oxide fuel cells (SOFC). One of the most representative perovskite-based SOFC anode material is lanthanum-doped $SrTiO_3$ (LST), because it shows good chemical stability, high electrical conductivity under very low oxygen partial pressures and stable performance under cycling condition [20]. LST powders were prepared by USP from aqueous solution of a metal nitrates [20]. The SOFC performances were improved by USP-synthesized LST due to increase in electrode area. In addition, the sintered LST body showed the dependence of electrical conductivity on La doping concentration under reduction atmosphere.

Bearing in mind these considerations, Co-based perovskites could be good candidates for supercapacitive applications with prolonged cyclability in comparison to carbon-based composites due to their mixed proton/electron conductivity and cycling stability. LSCO should be of wider voltage window than carbonaceous materials, with the possibility to interactively host the pseudocapacitive oxide, such as RuO_2. This could involve not only simple surface adsorption, but also full or partial incorporation into the oxide structure, like in the case of rare earth ruthenates. Its capacitor applications appear to be restricted to alkaline to neutral media, owing to the LSCO composition. Hence, this work aims to investigate supercapacitive potentials of pure LSCO and LSCO hydrothermally doped by RuO_2. Single-step USP was applied to synthesize LSCO, whereas the incorporation of RuO_2 into LSCO was performed by hydrothermal alkaline hydrolysis of ruthenium chloride.

2. Experimental

2.1. Synthesis of $La_{0.6}Sr_{0.4}CoO_3$ powder by ultrasonic spray pyrolysis

The synthesis of Co-based oxide, namely $La_{0.6}Sr_{0.4}CoO_3$ (LSCO), was performed within single-step USP procedure. The detailed USP synthesis procedure and prototype USP device are explained in Supplementary material (Fig. S1). As starting precursors aqueous solutions with 0.10 M concentration of $La(NO_3)_3 \cdot 6H_2O$ (99.9% rare earth oxide), $Sr(NO_3)_2$ (99%) and $Co(NO_3)_2$ (98%), all from Alfa Aeser, were used for the synthesis of LSCO.

2.2. Preparation of ruthenium oxide-impregnated LSCO nanocomposite

$LSCO/RuO_2$ (20 mass % RuO_2, nominal) composite was synthesized through simple chemical precipitation method. Water suspension of USP-synthesized $La_{0.6}Sr_{0.4}CoO_3$ powder and ruthenium chloride ($RuCl_3 \cdot H_2O$) were used as starting materials. LSCO powder was ultrasonically suspended for 30 min and the pH value of the magnetically stirred suspension was afterwards adjusted to 10 by 0.10 M KOH. With pH kept constant, 0.10 M water solution of $RuCl_3$ is added dropwise to the LSCO suspension and the stirring is continued for another 1 h. The resulting stable blackish precipitate was washed with distilled water and ethanol several times, and finally dried at 150 °C for 3 h.

3. Characterization techniques

3.1. Surface morphology and structural analysis

The morphology and elemental composition of LSCO and $LSCO/RuO_2$ powders were analyzed by scanning electron microscopy (SEM) and energy dispersive X-ray spectroscopy (EDS). A scanning electron microscope (Zeiss DSM 982 Gemini; Vega TS 5130 MM Tescan) was used to examine the appearance of obtained LSCO particles. In order to test the applicative potentials of LSCO-based materials in different capacitor electrolytes, SEM and EDS were performed upon exposition of LSCO powder to aqueous, alkaline and acid media. The synthesized powder was mixed with water, 0.10 M H_2SO_4 or 0.10 M KOH, stirred for 1 h, centrifuged and dried in air prior to SEM and EDS investigation. The elemental composition was determined by EDS with a Si(Bi) X-ray detector connected to the SEM and a multi-channel analyzer. The identification of elements was performed *via* the unique set of peaks from reflected X-ray spectrum.

Structural and phase analysis of the LSCO and $LSCO/RuO_2$ particles were examined by X-ray diffraction (XRD) measurements on Philips PW 1050 powder diffractometer at room temperature with Ni-filtered CuKα radiation ($\lambda = 1.54178$ Å) and scintillation detector within 10–82° 2θ range in steps of 0.05°, and scanning rate of 5 s per step.

3.2. Electrochemical measurements

Electrochemical properties of LSCO and $LSCO/RuO_2$ were studied by cyclic voltammetry (CV), electrochemical impedance spectroscopy (EIS) and galvanostatic charge-discharge (G-C/DC) tests. The electrochemical measurements were performed in a conventional three-electrode cell. A platinum foil and Hg/HgO/1M KOH electrode were used as counter and reference electrode, respectively. All potentials in the discussion are referred to the Hg/HgO electrode. The working electrode was glassy carbon (GC, Sigradur – Sigri, Elektrographite, GmbH, Germany) with the surface area of 0.39 cm^2 covered by a thin layer of LSCO or $LSCO/RuO_2$ according to the following procedure. 39 μL of LSCO or $LSCO/RuO_2$ water suspension (3 mg mL^{-1}) was added onto GC by micropipette. After 2 h of drying in air, the same volume of Nafion solution (100:1 *vs.* water), achieved by dissolving Nafion perfluorinated resin solution in 1 mL water, was added on top of the layer and left to additionally dry at room temperature. The thin Nafion film binds the investigated powders to GC substrate and provides necessary proton transport towards the electrode layer. The cell was purged with N_2 for 30 min prior to electrochemical measurements. An electrochemical work station (BioLogic SAS, SP-240, Grenoble, France) of potentiostat/galvanostat provided with corrosion and physical electrochemistry software was employed. The CV responses in 0.10 M KOH were checked at the scan rate of 50 mVs^{-1}. The specific capacitance, the most important indicator for the evaluation of electrode properties for supercapacitors [21,22], was calculated from the CV data according to the following Eq. (1):

$$C_s = \frac{1}{2m\upsilon(|Ea| + |Ec|)} \int_{Ec}^{Ea} I(E)dE \quad (1)$$

where C_s (F g^{-1}) is the specific capacitance, m (g) is the mass of the active material, I (E) is the current recorded during CV, υ (V s^{-1}) is the scan rate, and E_a and E_c (V) are low and high potential integration limits or the capacitive potential window.

EIS studies were carried out in the frequency range of 10^{-2}–10^{6} Hz by using 10 mV root mean square sinusoidal potential amplitude around open circuit reading (63.2, 75.1 and 68.8 mV for LSCO, LSCO/RuO_2 and RuO_2, respectively). The EIS data were fitted and analyzed by means of the equivalent circuit using the EC-Lab® software (version V11.16).

The cycle-life tests of the samples were analyzed by G-C/DC tests with the same laboratory equipment. Galvanostatically charged and discharged curves were measured at (50 μA) and high (0.50 mA) current densities until the 500 mV voltage range is spent. The specific capacitances were calculated from the following equation (2) [23,24]:

$$C = \frac{I\Delta t}{m\Delta E} \quad (2)$$

where C (F g^{-1}) is the specific capacitance, I (mA) represent the charge/discharge current, Δt (s) is the time required to spent the potential window, ΔE (V), and m (g) represents the mass of active material.

4. Results and discussion

4.1. SEM and EDS analysis

Morphology plays an important role in the electrochemical behavior of the porous materials since it should to allow maximal availability of active sites [25,26]. Morphology of the LSCO powder is presented in Fig. 1 by its typical SEM appearance. EDS composition is presented in Table 1. As-prepared LSCO powder is uniformly consisted of almost ideal spherical grains, with a sphere diameter in the range of 0.5–3 μm. EDS composition mapping was done on three spots at different spheres and the average value of these elemental compositions are listed in Table 1.

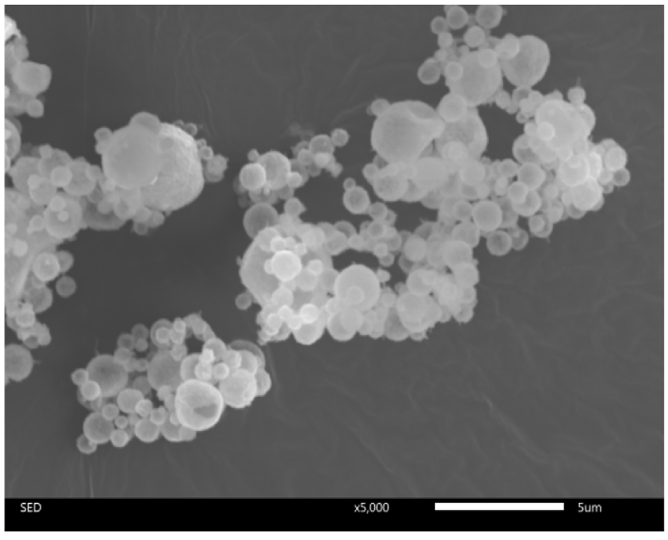

Fig. 1. Typical SEM microphotograph of $La_{0.6}Sr_{0.4}CoO_3$ powder synthesized by ultrasonic spray pyrolysis.

Table 1
EDS comparative analysis of LSCO powder in the pristine condition and after immersion in: water, alkaline and acid solution (at.%).

Element/*at. %*	*Powder*	*KOH*	*H_2SO_4*	*Water*
O	16,92	63.55	50.40	63.24
Sr	8.66	8.65	32.31	9.11
La	10.56	11.18	1.60	10.77
Co	16.92	16.62	15.17	16.60

The morphologies of LSCO powders exposed to different media are presented in Fig. 2. No significant changes in powder morphology of LSCO upon its exposure to water (Fig. 2a) or alkaline medium (Fig. 2b) were found. On the other hand, acid medium considerably violates the spherical structure, as seen in Fig. 2c.

LSCO appears chemically stable in alkaline solution, with unchanged spherical morphology and sphere diameter comparable to original LSCO powder. On the other hand, the SEM surface appearance of the powder upon exposure to acid solution is considerably different. There are no signs of uniform spherical structure. This structure was ruined in a high extent with simultaneous agglomeration of the material. The surface of agglomerates appears uniformly roughed, contrary to the extensively smooth surface of initial spheres.

EDS analysis results of LSCO powders exposed to 0.10 M KOH, 0.10 M H_2SO_4 and water are shown in Table 1, alongside with quantity analysis of LSCO powder obtained by USP method.

As seen in Table 1, the detected contents of La and Sr elements for LSCO powder are negligibly different from stoichiometric one of 3:2, the difference is even negligible due to the poor accuracy of EDS. The La:Sr ratio were 1.22, 1.18 and 1.30 for LSCO powder, LSCO in water and LSCO in KOH solution, respectively. It can be observed by comparing EDS values with LSCO powder in pristine condition from Table 1 that there is no dissolution of any component in KOH. Therefore, the LSCO powder is chemically stable and of preserved morphology in alkaline solution. On the other hand, drastic relative decrease in La and increase in Sr contents, as well as slight decrease of Co content, can be observed by exposition to acid solution (Table 1). The Sr:Co ratio was 1:2 in original LSCO powder, while it changed to 2:1 when it is in acidic environment. This proves that crystal lattice is destroyed and diverse into another type of crystal structure. It can be concluded that acidic environment dissolves La and Co from LSCO crystal structure, and hence changes not only its morphology, but also crystalline structure because of change in Sr:Co ratio.

The morphology of novel LSCO/RuO_2 material was also characterized by SEM and the images are shown in Fig. 3. Spherical structure of initial LSCO powder is maintained. Although LSCO/RuO_2 powder has the same spherical shape some changes of particle surface structure can be noticed. It appears that some additional particles are incorporated into the LSCO surface. We presume that these particles are to be RuO_2 on the surface of LSCO particle with size roughly around 2–3 nm. The enlarged view in Fig. 3b shows that supposed RuO_2 is uniformly arranged on the surface of LSCO spheres.

The averaged elemental composition of the grains was analyzed by EDS, confirming the Ru presence in the nanocomposite LSCO/RuO_2 powder.

From Table 2 it can be observed that avarage value of 2 at. % of ruthenium was detected in this powder. Spectrum show very small Sr content and it is below EDS detection limit. The mass % value of ruthenium oxide was calculated from at. % of ruthenium. The calculations returned 13 mass % of ruthenium oxide is incorporated into the LSCO. Hence, ruthenium oxide nanoparticles supported on LSCO surface was obtained by combined USP/hydrothermal synthesis.

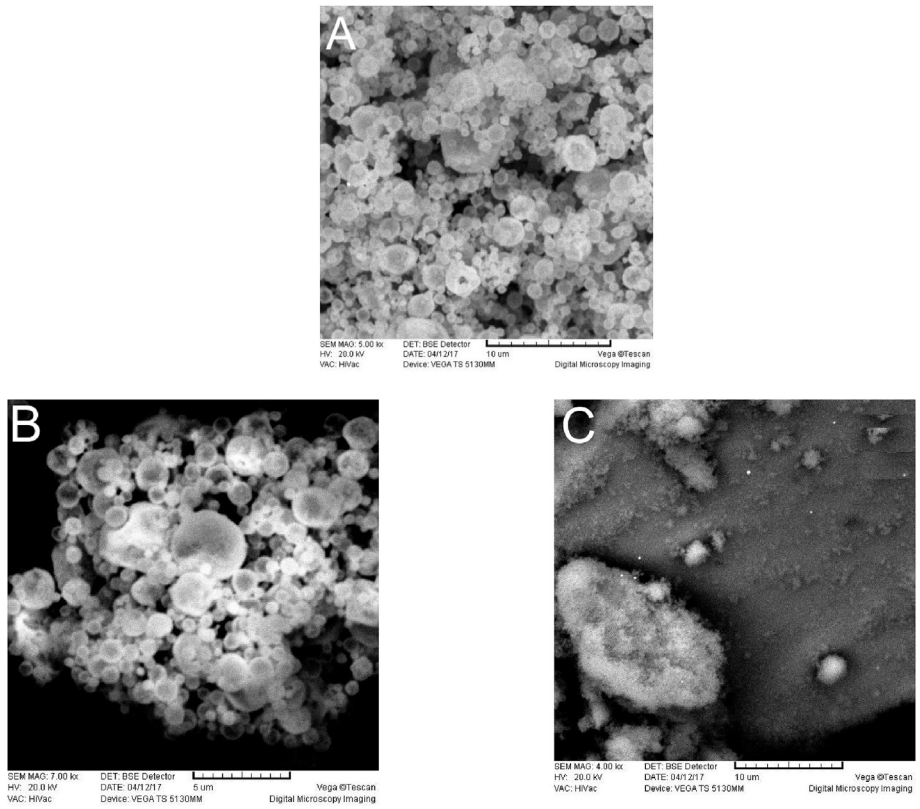

Fig. 2. SEM microphotographs of LSCO powder after immersion in: a) water, b) 0.10 M KOH and c) 0.10 M H_2SO_4.

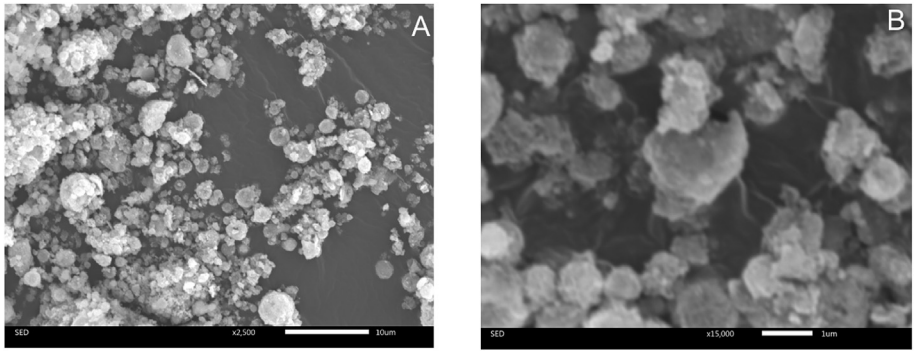

Fig. 3. SEM microphotographs of LSCO/RuO_2 powder: (a) general view and (b) magnified view.

Table 2
Elemental analysis of LSCO/RuO_2 nanocomposite from EDS measurements.

Element	*at. %*
O	80.22
Sr	–
La	5.61
Co	12.40
Ru	1.77

4.2. X-ray diffraction analysis

XRD patterns of LSCO and LSCO/RuO_2 powders are represented in Fig. 4. The crystal phases of both samples were in good agreement with the perovskite structure, derived from standard $La_{0.6}Sr_{0.4}CoO_3$ compound. The specific XRD peaks correspond to JCPDS card (JCPDS PDF No. 01-89-2528).

It can be seen in Fig. 4 that all of the XRD peaks related to LSCO are very sharp in the 2θ range of 10–80°, indicating highly crystalline nature of LSCO powder. Synthesized LSCO consists of single–phase with the rhombohedral crystal structure. For perovskites, as well as other crystalline materials, the variation in the crystal structure may lead to distinct electrocatalytic activities [27]. It was found that LSCO powder has a rhombohedral lattice typical for standard perovskite structure which can be indexed as R-3c space group symmetry (#161) [27]. Crystal structure may not have significant effect on the electrochemical activity. New diffraction peaks, such as Co_3O_4, La_2O_3, $La_3Ru_3O_{11}$ and K_2RuO_4, can be distinguished in the pattern of LSCO/RuO_2. Appearance of new XRD peaks can indicate that the nanoparticles of a new compound, as seen by SEM analysis as uniformly dispersed RuO_2 on the LSCO surface

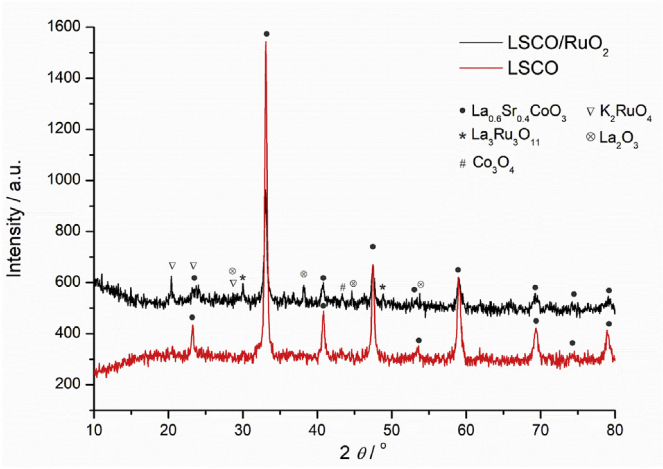

Fig. 4. XRD patterns of LSCO and LSCO/RuO_2 powders.

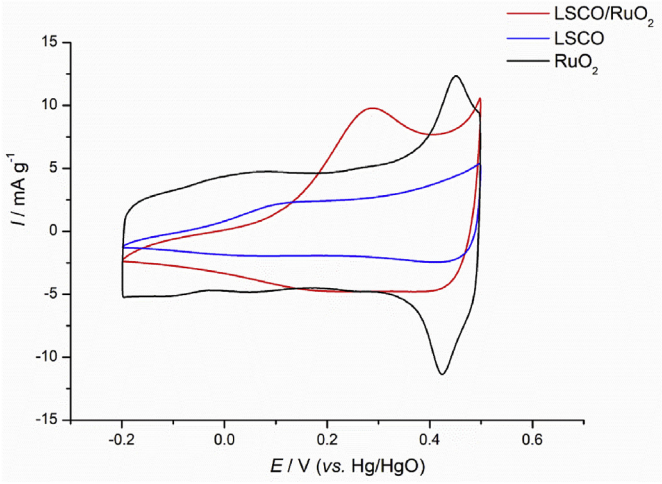

Fig. 5. Cyclic voltammograms of LSCO, LSCO/RuO_2 and RuO_2 at a scan rate of 50 mVs^{-1} in 0.10 M KOH; room temperature.

(Fig. 4b). Comparison of the intensity of basal most pronounced peak for LSCO at $2\theta = 33°$ (assigned 100%) to the intensities of new diffraction peaks for Ru-based phase revealed approximately normalized value of 28%, which indicates slight incorporation of Ru into crystal lattice.

The 2θ peaks at around 21.5, 23.1 and 29.2° were attributed to K_2RuO_4 phase from the JCPDS PDF No.01-051-1751, which was considered to be the result of partial incorporation of Ru ions into LSCO crystal lattice. It can also be confirmed by appearance of additional diffraction peaks at around $2\theta = 30$, 35.6 and 49.1° that was attributed to another ruthenate phase - $La_3Ru_3O_{11}$ (JCPDS PDF No.01-070-1086). This indicates the formation of very small amount of some new ruthenium compounds with lanthanum and potassium. Some weak peaks are also found at around 29.2, 38.1, 44.9 and 53.5° due to the presence of lanthanum oxide, La_2O_3, according to the JCPDS PDF No. 00-40-1279, which can be considered as a partial LSCO decomposition induced by doping of ruthenium. The appearance of very weak peak at $2\theta = 36.9°$ is an indication of Co_3O_4 phase in LSCO/RuO_2 sample. It is important to note that the poorly crystalline state/amorphous and hydrous RuO_2 particle may actually be related to absence of typical XRD peaks of RuO_2.

4.3. Electrochemical analysis and performances

Stable cyclic voltammograms (CV) of LSCO, LSCO/RuO_2 and pristine USP-synthesized RuO_2 thin layer on GC substrate, recorded at the scan rate of 50 mVs^{-1} in 0.10 M KOH are shown in Fig. 5.

The electrochemical capacitance is affected by two contributions, electrical double layer capacitance (ECDL) and pseudocapacitance (PC) [28]. It is known that unique capacitive features of RuO_2 in considerable portions come from PC due to reversible Ru(III)/Ru(IV) and Ru(IV)/Ru(VI) redox transitions [29]. The CV of pure RuO_2 shows the doublet of broad, weakly-pronounced, anodic and cathodic peaks around 50 and 300 mV, typically assignable to highly reversible Ru redox transitions. In addition, there is much sharper redox pair prior to oxygen evolution, which appears around 45. This pair is usually associated to adsorption/desorption of OH^- [29].

The shape of the CV curve of the LSCO-based materials is different, with fewer features, in comparison to the registered for RuO_2. The least features and lowest CV currents are registered in CV response of LSCO, indicating the lowest active surface area. Incorporation of RuO_2 into LSCO results in considerable increase in CV currents of LSCO, as registered for LSCO/RuO_2 powder at the potentials positive to 0.0 V. In the potential region of low currents, negative to 0.0 V, the influence of RuO_2 is not pronounced. Although being quite weak, the broad redox pair, with a shoulder-like anodic counterpart, can be distinguished for LSCO around 100 mV. On the other hand, LSCO/RuO_2 exhibits well-resolved anodic peak at 300 mV, with unclear cathodic counterpart. Instead, a constant discharging current is registered in the potential region for 400 down to 100 mV, of quite similar value to that of RuO_2. The corresponding feature of LSCO is roughly of twice lower discharging current. Finally, in the region of well-resolved OH adsorption/desorption of RuO_2, the moderate increase in anodic currents is found for LSCO and LSCO/RuO_2.

It can be assumed that RuO_2 enhances the capacitive response of LSCO in the potential region of the redox transition of the LSCO oxides. Besides intensification of the CV currents, the redox transitions of LSCO/RuO_2 is shifted to more anodic potentials with respect to LSCO and takes position tightly close to weakly-pronounced redox pair of RuO_2 positioned around 300 mV. It appears that not only RuO_2 promotes the capacitive response of LSCO, but also LSCO favors and enhances redox transition of Ru in higher oxidation states. These changes could be associated to the selective and localized replacement of Sr by Ru as reported in Table 2. The displacement also changes the ratio of earth to transition metal from nominally 1:1 (found 1.2:1) to a bit above 1:2.5. Simultaneously, La_2O_3 appears as a new phase (Fig. 4), which can improve the pseudocapacitive capabilities of the material by intensification of transition metals-related redox transitions. Tables 1 and 2 also report the considerably larger excess of oxygen in LSCO/RuO_2 with respect to water- or alkaline-treated LSCO, and especially acid-treated LSCO. This oxygen in excess can bond easier the H from OH^- in solution and improve the protonic conductivity of the oxides in LSCO/RuO_2.

The specific capacitance, C_s, of the samples was calculated by integrating the area delimited by CV curve according to the Eq. (2). The C_s calculated for LSCO/RuO_2 and LSCO are found to be 75.8 and 37.8 Fg^{-1}, respectively. The specific capacitance for USP-synthesized RuO_2 is 90.7 F g^{-1} (excluding the charge exchanged in OH adsorption/desorption region), which is in good agreement with the data reported in the literature [30]. The capacitance of LSCO was considerably increased by RuO_2. The Sr substitution by Ru leads to higher rates of redox reactions, resulting in an enhanced electrochemical performance [16], represented by well-pronounced anodic peak around 300 mV. Since the influence of RuO_2 is

registered mainly in the potential region of redox transitions (Fig. 5), we have calculated C_s values in the potential range from 0 to 350 mV, which excludes the region of poor capacitive response (negative to 0.0V). Calculated specific capacitance values are 43.8, 93.1 and 95.8 Fg^{-1} for LSCO, LSCO/RuO_2 and RuO_2, respectively. This reveals that the capacitance of LSCO/RuO_2 can even reach the value of pure RuO_2, although its loading is nominally only 20 mass % (or, as found: 13 mass % at the places where Ru replaces Sr). The capacitance of LSCO/RuO_2 is considerably higher with respect to that in whole CV potential range, whereas only slightly higher values are calculated for LSCO and RuO_2. This can be an additional indication of mutual catalytic effects and interactivity enhancement between LSCO and RuO_2, which concerns mainly the region of oxide redox transitions. In summary, if LSCO and LSCO/RuO_2 capacitances are compared, the value is more than doubled by RuO_2 incorporation, irrespective to the potential range of capacitance calculations.

According to the literature [31–33], registered capacitive behavior could be more like battery-type or capacitive-type. Battery-type relates more to diffusion-controlled process, whereas capacitor-type is due to surface-controlled process [32,33]. Since K^+ intercalation into pure ruthenium dioxide is not reported so far, it can be concluded that LSCO/RuO_2 material possess redox Ru/Co redox transition process characteristics in the presence of OH^-, *i.e.*, capacitive-type response with negligible diffusion capacitance contribution, similar to the response of $Ni(OH)_2$ [31].

High C_s values of pseudocapacitors is attributed to the appropriate porous metal oxide structure with high specific surface area, which increase the rates of pseudocapacitive Faradaic reactions [6,34]. For LSCO/RuO_2 sample, the addition of ruthenium oxide makes the surface of LSCO spheres rougher (Fig. 3), which increases the specific surface area. In general, higher specific surface area and mesoporous structure leads to easier and more efficient transport of both electrons and protons, which affects redox reactions to take place at high rates [6,34,35]. Therefore, nanoparticles of RuO_2 at the surface of LSCO spheres can affect storage efficiency of novel LSCO/RuO_2 material by increasing the surface area of the spheres, while LSCO interactively enhances the redox transitions of Ru species. In order to distinguish the mentioned different contributions to increased capacitance of LSCO/RuO_2, impedance measurements (EIS) were performed at 200 mV – the potential at which LSCO capacitive features are developed, but also pure RuO_2 and LSCO/RuO_2 express similar values of both charging and discharging currents (Fig. 5).

Fig. 6 shows Nyquist plots of the LSCO and LSCO/RuO_2 samples and USP-synthesized RuO_2. The presented plots consist of two parts: defined semicircle in the high-frequency region for LSCO and LSCO/RuO_2 (magnified in the inset of Fig. 6) and a capacitive straight line in the low-frequency region. Based on the impedance plot shape similar to those in Fig. 6, Jain and Tripathi suggested that the supercapacitive material can show high resistance at higher frequencies followed by pseudocapacitance and double-layer capacitance response [36]. In order to check the origin of the origin of high-frequency semicircle, the EIS response is checked at other two potentials (−400 and 300 mV), at cathodic and anodic side with respect to 200 mV (data not shown). The semicircle diameter is found to increase considerably while the potential is shifted anodically. This indicates that the semicircle relates rather to the Faradaic process than to resistance of the material. According to this assumption, fitting of the EIS data was accomplished by using the equivalent electrical circuit shown as the inset of Fig. 6, which EIS data are presented by lines.

Nyquist plots of LSCO and LSCO/RuO_2 samples before and after 300 cycles of charge/discharge are presented in Supplementary material in Fig. S2. Both Nyquist plots, before and after cycling, have

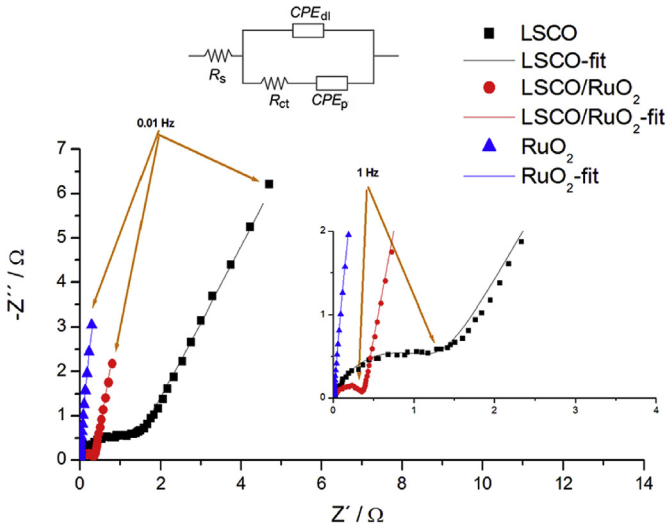

Fig. 6. Nyquist plots of LSCO, LSCO/RuO_2 and RuO_2 in 0.10 M KOH at 200 mV. Experimental (symbols) and fitting results (lines) of impedance data with adopted equivalent electrical circuit (inset).

a semicircle and a straight line at high and low frequencies, respectively. In high frequency region, a semicircle is observed for LSCO and LSCO/RuO_2 with the diameters representing the charge-transfer resistance (R_{ct}), assignable to the redox transitions [21] of Co and/or Ru species in LSCO and LSCO/RuO_2. After 300 cycles, the semicircle is less pronounced for both LSCO and LSCO/RuO_2. No-semicircle and capacitive-like response is registered for pure RuO_2, since redox transitions of Ru are rather fast to show clearly the time constant on the investigated frequency range. Hence, the simple equivalent circuit, consisted of R_s and constant phase element (CPE_p) in series, was used to fit RuO_2 data. The double layer charging/discharging is represented also by a constant phase element, CPE_{dl}, in parallel to R_{ct}. Pseudocapacitance is represented by CPE_p.

The double layer capacitance, C_{dl}, can be calculated from CPE and interfacial parameters by following equation [37–39]:

$$C_{dl} = Y_0(w_{max})^{n-1} \quad (4)$$

where ω_{max} is the angular frequency for the maximum of imaginary impedance. On the other hand, pseudocapacitance, C_p, can be calculated form CPE_p parameters using the equation for the case of series of CPE and R [40]:

$$C_p = \left[Y_0\left(R_s^{-1} + R_{ct}^{-1}\right)^{n-1}\right]^{1/n} \quad (5)$$

Goodness of fit by the proposed EEC is judged through three basic criteria to evaluate the general accuracy of the fit: visual fit to Nyquist plots, chi-squared below 10^{-4} and low relative standard errors for the parameter values of every circuit element (below 10%). The fitting results of charge-transfer resistance and specific capacitance are presented in Table 3.

The impedance spectrum of pure RuO_2 electrode is composed of vertical line in both low and high frequency regions almost parallel to the imaginary axis and indicates capacitive behavior (Fig. 7). According to literature, typical rutile structure of RuO_2 in hydrous state has pseudocapacitive response due to conversion of Ru(III)/Ru(IV) that is highly reversible reaction [29]. Recent study of Chalupczok et al. explained behavior of RuO_2 in alkaline solution and propose a surface species $Ru(OH)_3 \cdot RuO_2$ that is able to directly bind

Table 3
Fitting values of charge-transfer resistance and specific capacitance of LSCO, LSCO/RuO_2 and RuO_2 for supercapacitor applications.

Sample	C_{dl}/Fg^{-1}	C_p/Fg^{-1}	R_{ct}/Ωcm^2
LSCO	0.28	23.81	1343
LSCO/RuO_2	0.53	80.35	737
RuO_2	–	94.45	–

Table 4
A comparison among specific capacitances of LSCO, LSCO/RuO_2 and RuO_2 obtained by using G-C/CD measurements.

Sample	G-C/DC	
	50 μA	500 μA
LSCO	44.82	32.53
LSCO/RuO_2	92.72	100.60
RuO_2	111.70	/

hydroxyl ions [29]. Therefore, the EIS results of RuO_2 showed very high value of specific capacitance C_s, of 94.45 Fg^{-1}, which agrees with the value calculated from CV.

LSCO and LSCO/RuO_2 show mainly pseudocapacitive behavior, since electrical double layer capacitance, C_{dl}, is roughly 0.1% of C_p [9,41]. The roughening of the LSCO sphere surfaces by RuO_2 is seen as doubled value of C_{dl} of LSCO/RuO_2 with respect to LSCO. Similarly, R_{ct} of LSCO is almost twice of that for LSCO/RuO_2 due to slower redox reactions of transition metals. However, the pseudocapacitance is almost 3.5 times higher for LSCO/RuO_2, while CV responses showed only 2-fold increase, which is also found for C_{dl} from EIS data. This difference between EIS and CV data is in accordance with the conclusion that capacitive performance is improved by RuO_2 incorporation dominantly due to enhanced redox transitions (above 0.0 V). In the region of low capacitive currents (below 0.0 V), the double layer capacitive properties dominate the CV response.

In order to better understand applicability and especially the stability of LSCO and LSCO/RuO_2 as potential supercapacitor electrode material, galvanostatic charge-discharge (G-C/DC) curves were measured in 0.10 M KOH electrolyte at different C/DC currents of 50 and 500 μA. The results are shown in Fig. 7 along with G-C/DC curves of pristine RuO_2 at 50 μA. The shape of the G-C/DC curves show some deviation from linearity due to typical pseudocapacitive properties as discussed above [22,42]. Since the most pronounced pseudocapacitive behavior is reserved for pure RuO_2, its ability to store/release more charge in a narrow potential range, which disturbs full linearity, is seen in 0.1–0.35 V range. Note that inflections related to the changes in the slope correlate to the positions of the CV peaks assigned to redox transitions of Ru. Although the corresponding peaks for LSCO and LSCO/RuO_2 are also distinguished, the G-C/DC is more linear for these samples than for RuO_2 (Fig. 7a). It could be that transition from poor to capacitive response due to redox transitions slower than for RuO_2 at 0.0 V causes the more uniform changes in potential during G-C/DC actuation [43]. It is found that LSCO/RuO_2 exhibited good stability both at 50 and 500 μA C/D current (Fig. 7b) during 300 cycles.

The average specific capacitance (C_s, Fg^{-1}) from the G-C/DC curves was calculated according to Eq. (2). Table 4 shows a comparison between the specific capacitance of LSCO, LSCO/RuO_2 and RuO_2 registered at different currents by G-C/DC experiments.

The calculated specific capacitance for LSCO at 50 and 500 μA are 44.8 and 32.5 Fg^{-1}, respectively, with typical lower values in conditions of faster C/D [44–46]. On the other hand, specific capacitances for LSCO/RuO_2 are of different trend: 92.7 (50 μA) and 100.6 (500 μA) Fg^{-1}. This could be caused by the arrangement of the components within the composite as indicated by Fig. 3 – RuO_2 covers the LSCO spheres, thus facing directly the electrolyte and being readily available for the fast C/D. During the slow C/D, the response of less conductive LSCO from the core is taking place too, thus decreasing the average capacitance of the LSCO/RuO_2 composite.

Fig. 7b shows that LSCO/RuO_2, although being of superior capacitive performances with respect to LSCO that almost reach the RuO_2 performances, loses to some small extent the initial charging/discharging capabilities. In order to define the stability of the investigated materials, the long-term cyclability was tested. Fig. 8 summarizes the registered capacitive performances along with the cyclability projections.

Besides confirmed increase in capacitance, Fig. 8 additionally indicates that RuO_2 improves the cycling stability of LSCO (the 50% decrease in capacitance of LSCO is improved to only 10% decrease for LSCO/RuO_2 during 300 cycles). Under the same cycling conditions, no loss of the stability was found for pristine RuO_2 (the data are randomly distributed within shaded zone in Fig. 8). In addition, LSCO/RuO_2 appears less sensitive to cycling limits. While the limits are similar in CV and G-C/DC to gain the average capacitance, EIS gives the differential capacitance at open circuit potential close to redox transitions of oxides. The lower capacitance values from EIS indicate the requirement of the full development of redox

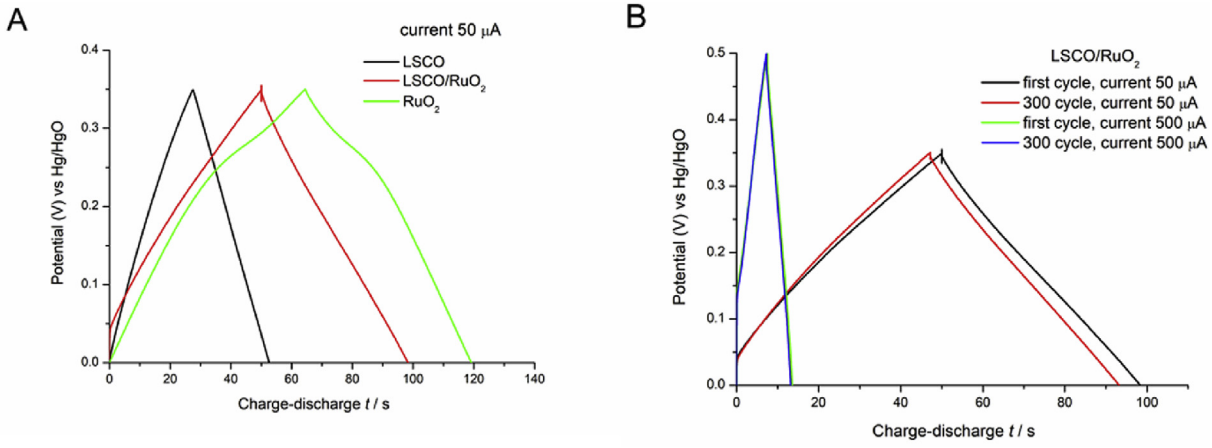

Fig. 7. Galvanostatic charge-discharge (G-C/DC) curves at different current densities: a) 50 μA of LSCO, LSCO/RuO_2 and RuO_2 and b) 50 and 500 μA of LSCO/RuO_2 in 0.10M KOH; room temperature.

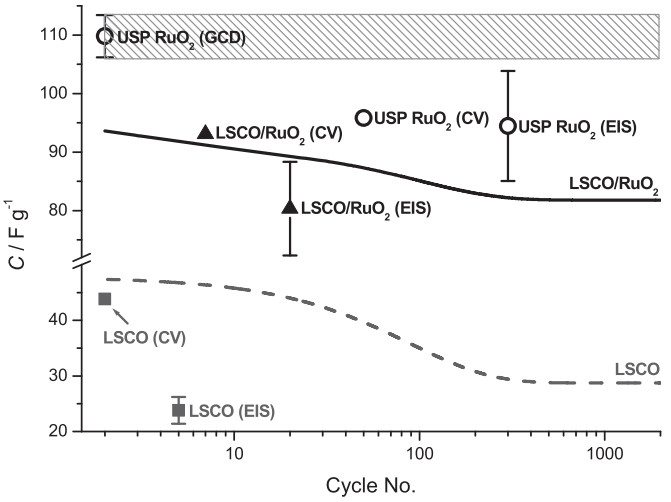

Fig. 8. G-C/DC cycling stability of LSCO/RuO_2, LSCO and pristine RuO_2 at the current of 50 μA; specific capacitance gained by different techniques are given by symbols with corresponding standard deviations.

transitions in a wider potential range. The differential capacitance by EIS of LSCO/RuO_2 is close to the average values gained by CV and G-C/DC, while the value from EIS for LSCO is even below the limiting average G-C/DC value from cyclability. It can be due to much faster oxide redox transitions for LSCO/RuO_2 as indicated by R_{ct} from EIS. Consequently, pseudocapacitance performances can develop in moderate polarization since fast redox transitions induces LSCO/RuO_2 charging state close to non-polarizable electrode.

Considering all previous investigation from the microstructure (SEM, EDS and XRD) to electrochemical performances (CV, EIS and G-C/DC) the LSCO/RuO_2 shows superior characteristics with respect to pure LSCO. The results are related to mutual promotion of the pseudocapacitive redox transitions of oxides, both RuO_2 and from LSCO. Consequently, registered capacitance of LSCO/RuO_2 is close to that of pristine RuO_2 with a loading of only 20 mass% of RuO_2 in LSCO. Beside the increase in specific capacitance, reversible charge-discharge performances are more stable LSCO/RuO_2 than for LSCO and in the required potential window this electrode has supercapacitor characteristics.

5. Conclusion

Lanthanum strontium cobalt oxide, $La_{0.6}Sr_{0.4}CoO_3$ (LSCO), have been successfully synthesized *via* single step USP technique and hydrothermally doped with RuO_2. We investigated the RuO_2 effect on the structure and morphology of LSCO/RuO_2, as well as supercapacitive performances of LSCO and LSCO/RuO_2 composites. The LSCO powder had a homogenous morphology consisted of almost ideal spheres. LSCO was chemically stable in alkaline solution while upon exposure to acidic environment evident changes in morphology and crystalline structure due to La dissolution were observed. Upon impregnation by RuO_2, spherical structure of initial LSCO powder was maintained, with RuO_2 nanoparticles supported on LSCO surface with the size around 2−3 nm. It appears that Ru replaces Sr in LSCO, since no Sr detected in LSCO/RuO_2.

One can assume that RuO_2 enhanced the capacitive response of LSCO and *vice versa* LSCO favors and enhance redox transition of Ru in higher oxidation states. This means that Sr replacement by Ru leads to higher rates of redox reactions improving pseudocapacitive performances of LSCO/RuO_2 composite. The displacement changes the ratio of earth to transition metal resulting in the appearance of new phases in diffractogram, such as La_2O_3, that can also improve the electrochemical performances. Therefore, RuO_2 nanoparticles can also affect on specific capacitance of LSCO/RuO_2 material by increasing the specific surface area of spheres. According to impedance measurements, the semicircle observed in the high frequency region represents charge-transfer resistance that is related to the redox transitions of LSCO and LSCO/RuO_2 composites. Notable difference between EIS and CV pseudocapacitance values can be explained that capacitive performances are dominantly improved by RuO_2 incorporation in the potential range above 0.0 V. The charging/discharging curves for LSCO and LSCO/RuO_2 composites are more linear than pristine RuO_2. Although LSCO/RuO_2 material exhibits superior capacitive response with respect to LSCO and almost close to pure RuO_2, LSCO/RuO_2 loses to some small extent the initial charging/discharging performances. From long-term cyclability LSCO/RuO_2 appears to be less sensitive than LSCO. Therefore, LSCO/RuO_2 composite has enhanced pseudocapacitive properties with good rate capability and better performance with respect to LSCO, which is related to a mutual promotion of pseudocapacitive redox transitions between RuO_2 and LSCO.

Acknowledgement

This work was supported by the Ministry of Education, Science and Technological Development of the Republic of Serbia (Grant No. 172060). We would like to thank the Ministry and DAAD, Germany, for the funding of Project No.:57334757.

Appendix A. Supplementary data

Supplementary data to this article can be found online at https://doi.org/10.1016/j.electacta.2019.134721.

References

[1] J. Deng, L. Kang, G. Bai, Y. Li, P. Li, X. Liu, Y. Yang, F. Gao, W. Liang, Solution combustion synthesis of cobalt oxides (Co3O4 and Co3O4/CoO) nanoparticles as supercapacitor electrode materials, Electrochim. Acta 132 (2014) 127−135, https://doi.org/10.1016/j.electacta.2014.03.158.

[2] Y. Cao, B. Lin, Y. Sun, H. Yang, X. Zhang, Symmetric/Asymmetric supercapacitor based on the perovskite-type lanthanum cobaltate nanofibers with Sr-substitution, Electrochim. Acta 178 (2015) 398−406, https://doi.org/10.1016/j.electacta.2015.08.033.

[3] A. Subasri, K. Balakrishnan, E.R. Nagarajan, V. Devadoss, A. Subramania, Development of 2D La(OH)3/graphene nanohybrid by a facile solvothermal reduction process for high-performance supercapacitors, Electrochim. Acta 281 (2018) 329−337, https://doi.org/10.1016/j.electacta.2018.05.142.

[4] S. Arunachalam, B. Kirubasankar, V. Murugadoss, D. Vellasamy, S. Angaiah, Facile synthesis of electrostatically anchored Nd(OH)3 nanorods onto graphene nanosheets as a high capacitance electrode material for supercapacitors, New J. Chem. 42 (2018) 2923−2932, https://doi.org/10.1039/c7nj04335j.

[5] K. Balakrishnan, M. Kumar, S. Angaiah, Synthesis of polythiophene and its carbonaceous nanofibers as electrode materials for asymmetric supercapacitors, Adv. Mater. Res. 938 (2014) 151−157. 10.4028/www.scientific.net/amr.938.151.

[6] R.B. Rakhi, W. Chen, D. Cha, H.N. Alshareef, Substrate dependent self-organization of mesoporous cobalt oxide nanowires with remarkable pseudocapacitance, Nano Lett. 12 (2012) 2559−2567, https://doi.org/10.1021/nl300779a.

[7] M. Wohlfahrt-Mehrens, J. Schenk, P.M. Wilde, E. Abdelmula, P. Axmann, J. Garche, New materials for supercapacitors, J. Power Sources 105 (2002) 182−188, https://doi.org/10.1016/S0378-7753(01)00937-5.

[8] H.S. Nam, K.S. Jang, J.M. Ko, Y.M. Kong, J.D. Kim, Electrochemical capacitance of nanoporous hydrous RuO2 templated by anionic surfactant, Electrochim. Acta 56 (2011) 6459−6463, https://doi.org/10.1016/j.electacta.2011.05.008.

[9] Y. Cao, B. Lin, Y. Sun, H. Yang, X. Zhang, Structure, morphology and electrochemical properties of LaxSr1-xCo0.1Mn0.9O3-δ perovskite nanofibers prepared by electrospinning method, J. Alloy. Comp. 624 (2015) 31−39, https://doi.org/10.1016/j.jallcom.2014.10.178.

[10] Y. Liu, Y. Jiao, B. Yin, S. Zhang, F. Qu, X. Wu, Enhanced electrochemical performance of hybrid SnO2@MOx (M = Ni, Co, Mn) core−shell nanostructures grown on flexible carbon fibers as the supercapacitor electrode materials, J. Mater. Chem. A. 3 (2015) 3676−3682, https://doi.org/10.1039/C4TA06339B.

[11] K.M. Lin, K.H. Chang, C.C. Hu, Y.Y. Li, Mesoporous RuO2 for the next generation supercapacitors with an ultrahigh power density, Electrochim. Acta 54 (2009) 4574–4581, https://doi.org/10.1016/j.electacta.2009.03.058.
[12] S. Arunachalam, B. Kirubasankar, E. Rajagounder Nagarajan, D. Vellasamy, S. Angaiah, A facile chemical precipitation method for the synthesis of Nd(OH) 3 and La(OH) 3 nanopowders and their supercapacitor performances, Chemistry 3 (2018) 12719–12724, https://doi.org/10.1002/slct.201803151.
[13] K. Singh, B. Kirubasankar, S. Angaiah, Synthesis and electrochemical performance of P2-Na0.67AlxCo1-xO2 ($0.0 \leq \times \leq 0.5$) nanopowders for sodium-ion capacitors, Ionics (Kiel) 23 (2017) 731–739, https://doi.org/10.1007/s11581-016-1821-z.
[14] X.W. Wang, Q.Q. Zhu, X.E. Wang, H.C. Zhang, J.J. Zhang, L.F. Wang, Structural and electrochemical properties of La0.85Sr0.15MnO3powder as an electrode material for supercapacitor, J. Alloy. Comp. 675 (2016) 195–200, https://doi.org/10.1016/j.jallcom.2016.03.048.
[15] J.S. Park, W.H. Chung, H.S. Kim, Y.B. Kim, Rapid fabrication of chemical-solution-deposited La0.6Sr0.4CoO3-d thin films via flashlight sintering, J. Alloy. Comp. 696 (2017) 102–108, https://doi.org/10.1016/j.jallcom.2016.11.074.
[16] P.M. Wilde, T.J. Guther, R. Oesten, J. Garche, Strontium ruthenate perovskite as the active material for supercapacitors, J. Electroanal. Chem. 461 (1999) 154–160, https://doi.org/10.1016/S0022-0728(98)00179-X.
[17] K. Hwang, H. Lee, Preparation of epitaxially grown LaSrCoO3 thin films on SrTiO3(100) substrates by the dipping-pyrolysis process, J. Mater. Sci. 35 (2000) 6209–6212.
[18] K. Hwang, H. Lee, S. Min, B. Kang, Epitaxially grown LaSrCoO3 thin films on various substrates by the sol-gel method, J. Sol. Gel Sci. Technol. 3 (2000) 175–180, https://doi.org/10.1023/A:1008725205747.
[19] M. Losurdo, A. Sacchetti, P. Capezzuto, G. Bruno, Optical and electrical properties of nanostructured LaCoO3 thin films, Appl. Phys. Lett. 87 (2005), 061909.
[20] K. Genji, K. Myoujin, T. Kodera, T. Ogihara, Synthesis and electrical properties of La doped SrTiO3 powders by ultrasonic spray pyrolysis, Key Eng. Mater. 582 (2013) 115–118.
[21] J. Lü, Y. Zhang, Z. Lü, X. Huang, Z. Wang, X. Zhu, B. Wei, A preliminary study of the pseudo-capacitance features of strontium doped lanthanum manganite, RSC Adv. 5 (2015) 5858–5862, https://doi.org/10.1039/C4RA13583K.
[22] P.S. Gaikar, S.T. Navale, V.V. Jadhav, P.V. Shinde, D.P. Dubal, P.R. Arjunwadkar, F.J. Stadler, M. Naushad, A.A. Ghfar, R.S. Mane, A simple wet-chemical synthesis, reaction mechanism, and charge storage application of cobalt oxide electrodes of different morphologies, Electrochim. Acta 253 (2017) 151–162, https://doi.org/10.1016/j.electacta.2017.09.039.
[23] B. Kirubasankar, V. Murugadoss, S. Angaiah, Hydrothermal assisted: in situ growth of CoSe onto graphene nanosheets as a nanohybrid positive electrode for asymmetric supercapacitors, RSC Adv. 7 (2017) 5853–5862, https://doi.org/10.1039/c6ra25078e.
[24] B. Kirubasankar, V. Murugadoss, J. Lin, T. Ding, M. Dong, H. Liu, J. Zhang, T. Li, N. Wang, Z. Guo, S. Angaiah, In situ grown nickel selenide on graphene nanohybrid electrodes for high energy density asymmetric supercapacitors, Nanoscale 10 (2018) 20414–20425, https://doi.org/10.1039/c8nr06345a.
[25] P.M. Shafi, N. Joseph, A. Thirumurugan, A.C. Bose, Enhanced electrochemical performances of agglomeration-free LaMnO3 perovskite nanoparticles and achieving high energy and power densities with symmetric supercapacitor design, Chem. Eng. J. 338 (2018) 147–156, https://doi.org/10.1016/j.cej.2018.01.022.
[26] D. Thiele, E. Lopez-Camacho Colmenarejo, B. Grobety, A. Züttel, Synthesis of carbon nanotubes on La0.6Sr0.4CoO3 as substrate, Diam. Relat. Mater. (2009), https://doi.org/10.1016/j.diamond.2008.08.001.
[27] J. He, J. Sunarso, Y. Zhu, Y. Zhong, J. Miao, W. Zhou, Z. Shao, High-performance non-enzymatic perovskite sensor for hydrogen peroxide and glucose electrochemical detection, Sens. Actuators B Chem. 244 (2017) 482–491, https://doi.org/10.1016/j.snb.2017.01.012.
[28] J. Zhang, J. Ma, L.L. Zhang, P. Guo, J. Jiang, X.S. Zhao, Template synthesis of tubular ruthenium oxides for supercapacitor applications, J. Phys. Chem. C 114 (2010) 13608–13613, https://doi.org/10.1021/jp105146c.
[29] S. Chalupczok, P. Kurzweil, H. Hartmann, C. Schell, The redox chemistry of ruthenium dioxide: a cyclic voltammetry study—review and revision, Int. J. Electrochem. 2018 (2018), 1273768, https://doi.org/10.1155/2018/1273768.
[30] T. Audichon, B. Guenot, S. Baranton, M. Cretin, C. Lamy, C. Coutanceau, Effect of the annealing atmosphere on the electrochemical properties of RuO2nano-oxides synthesized by the Instant Method, Appl. Catal. B Environ. 218 (2017) 385–397, https://doi.org/10.1016/j.apcatb.2017.06.081.
[31] B. Kirubasankar, P. Palanisamy, S. Arunachalam, V. Murugadoss, S. Angaiah, 2D MoSe 2 -Ni(OH) 2 nanohybrid as an efficient electrode material with high rate capability for asymmetric supercapacitor applications, Chem. Eng. J. 355 (2019) 881–890, https://doi.org/10.1016/j.cej.2018.08.185.
[32] B. Kirubasankar, S. Vijayan, S. Angaiah, Sonochemical synthesis of a 2D-2D MoSe 2/graphene nanohybrid electrode material for asymmetric supercapacitors, Sustain. Energy Fuels 3 (2019) 467–477, https://doi.org/10.1039/c8se00446c.
[33] J. Liu, J. Wang, C. Xu, H. Jiang, C. Li, L. Zhang, J. Lin, Z.X. Shen, Advanced energy storage devices: basic principles, analytical methods, and rational materials design, Adv. Sci. 5 (2018), https://doi.org/10.1002/advs.201700322.
[34] B. Bhujun, M.T.T. Tan, A.S. Shanmugam, Evaluation of aluminium doped spinel ferrite electrodes for supercapacitors, Ceram. Int. 42 (2016) 6457–6466, https://doi.org/10.1016/j.ceramint.2015.12.118.
[35] Y. Liu, J. Dinh, M.O. Tade, Z. Shao, Design of perovskite oxides as anion-intercalation-type electrodes for supercapacitors: cation leaching effect, ACS Appl. Mater. Interfaces 8 (2016) 23774–23783, https://doi.org/10.1021/acsami.6b08634.
[36] A. Jain, S.K. Tripathi, Experimental studies on high-performance supercapacitor based on nanogel polymer electrolyte with treated activated charcoal, Ionics (Kiel) 19 (2013) 549–557, https://doi.org/10.1007/s11581-012-0782-0.
[37] F.M.C.H. Hsu, Concerning the conversion of the constant phase element parameter Y0 into a capacitance, Corrosion 57 (2001) 747–748. https://doi.org/10.5006/1.3280607.
[38] M. Slayters-Renbach, Impedances of electrochemical systems: terminology, nomenclature and representation, Pure Appl. Chem. 66 (1994) 1831–1891. https://doi.org/10.1351/pac199466091831.
[39] O.E. Mark, T. Bernard, Electrochemical impedance spectroscopy, in: Electrochem. Impedance Spectrosc., John Wiley & Sons, Inc., Hoboken, New Jersey, 2008, p. 1.
[40] P. Córdoba-Torres, T.J. Mesquita, R.P. Nogueira, Relationship between the origin of constant-phase element behavior in electrochemical impedance spectroscopy and electrode surface structure, J. Phys. Chem. C 119 (2015) 4136–4147, https://doi.org/10.1021/jp512063f.
[41] D. Li, X. Guo, H. Song, T. Sun, J. Wan, Preparation of RuO2 -TiO2/Nano-graphite composite anode for electrochemical degradation of ceftriaxone sodium, J. Hazard Mater. 351 (2018) 250–259, https://doi.org/10.1016/j.jhazmat.2018.03.007.
[42] G.X. Wang, B.L. Zhang, Z.L. Yu, M.Z. Qu, Manganese oxide/MWNTs composite electrodes for supercapacitors, Solid State Ion. 176 (2005) 1169–1174, https://doi.org/10.1016/j.ssi.2005.02.005.
[43] I.N. Bkrey, A.A. Moniem, Flexible laser reduced graphene oxide/MnO 2 electrode for supercapacitor applications, Int. J. Chem. Nucl. Metall. Mater. Eng. 8 (2014) 829–835.
[44] S. Chen, J. Zhu, X. Wang, One-step synthesis of graphene– cobalt hydroxide nanocomposites and their electrochemical properties, J. Phys. Chem. C 114 (2010) 11829–11834, https://doi.org/10.1021/jp1048474.
[45] S.K. Meher, G.R. Rao, Ultralayered Co3O4 for high-performance supercapacitor applications, J. Phys. Chem. C 115 (2011) 15646–15654, https://doi.org/10.1021/jp201200e.
[46] T. Brousse, D. Belanger, J.W. Long, To Be or not to Be pseudocapacitive? J. Electrochem. Soc. 162 (2015) A5185–A5189, https://doi.org/10.1149/2.0201505jes.

View publication stats